PCCP

ROYAL SOCIETY OF CHEMISTRY

PAPER

View Article Online
View Journal | View Issue

Check for updates

Cite this: *Phys. Chem. Chem. Phys.*, 2024, **26**, 24849

Infrared-driven dynamics and scattering mechanisms of NO radicals with propane and butane: impacts of pseudo Jahn–Teller effects†

P. Garrett Burroughs, W. Churchill Wilkinson, Ellora Majumdar, Jacob D. Bole, Reeva Subedi, Joshua T. Kerrigan and Nathanael M. Kidwell *

Received 2nd June 2024,
Accepted 10th September 2024

DOI: 10.1039/d4cp02254h

rsc.li/pccp

The topology of multidimensional potential energy surfaces defines the bimolecular collision outcomes of open–shell radicals with molecular partners. Understanding these surfaces is crucial for predicting the inelastic scattering and chemical transformations of increasingly complex radical–molecule collisions. To characterize the inelastic scattering mechanisms of nitric oxide (NO) radicals with large alkanes, we generated the collision complexes comprised of NO with propane or *n*-butane. The infrared action spectroscopy and infrared-driven dynamics of NO–propane and NO–(*n*-butane) collision complexes in the CH stretch region were recorded, while also comparing the results to the analogous experiments carried out for NO–CH_4 and NO–ethane. The infrared spectroscopy is analyzed using rovibrational simulations to characterize the transition bands and to determine the vibrational predissociation lifetimes of NO–propane and NO–(*n*-butane). Due to pseudo Jahn–Teller dynamics, the NO–propane and NO–(*n*-butane) decay mechanisms from IR activation appear similar to those for NO–ethane previously reported from this laboratory (J. P. Davis *et al. Faraday Discuss.*, 2024, **251**, 262–278). Furthermore, the NO ($X^2\Pi$, $v'' = 0$, J'', F_n, Λ) product state distributions from NO–alkane fragmentation reveal a strong electron-spin polarization and a propensity for NO products to rotate in the plane of the π^* molecular orbital, yielding mechanistic insights into the inelastic scattering outcomes. We hypothesize that a geometric phase may be present, impacting the relative population distributions, in addition to the accessible pathway timescales.

Introduction

In the troposphere, nitric oxide (NO) is a prevalent byproduct from anthropogenic sources including motor vehicles, industrial and commercial fuel combustion, and utilities.[1] As such, interactions between NO and other atmospherically relevant species including noble gases, diatomics and polyatomic molecules are of significant interest. In particular, the bimolecular collision of NO and alkanes are pivotal for understanding complex environmental processes that affect ozone formation, acid rain decomposition, and secondary particulate matter generation.[2] On a fundamental level, preparing reactants with isomer- and quantum-state specificity holds the promise to provide detailed information on the accessible reaction pathways. It has been shown that the reactants' impact collision geometries play a crucial role in determining the outcomes from inelastic scattering and chemical transformations.[3–7]

In this work, we combine infrared spectroscopy with velocity map imaging to reveal the inelastic scattering outcomes between NO and propane or *n*-butane. First, we characterize the collision complex between NO and the target alkane along the bimolecular collision pathway. Then, we photoinitiate fragmentation using infrared activation and characterize the energy flow mechanisms with state-to-state resolution. As mentioned, the bimolecular collision pathways between NO and alkanes relies upon the impact geometry, which determines whether the outcomes are reactive or nonreactive. As the alkane chain length is increased, there is a simultaneous increase in the possible collision orientations and therefore the available mechanisms due to the greater number of interaction sites. Furthermore, the intermolecular interactions and the resulting collision outcomes are influenced by the activation of either collision partner in certain degrees of freedom (*e.g.*, vibration, rotation, and/or translation) before impact. Indeed, the specific conditions under which these collisions occur may either accelerate or inhibit chemical reactions and/or energy-exchange mechanisms.

Earlier studies on NO–alkane complexes have examined the vibronic spectroscopy of NO–methane, ethane, propane, and *n*-butane.[8] Wright *et al.* used (1 + 1) resonance-enhanced

---

Department of Chemistry, The College of William & Mary, Williamsburg, VA 23187-8795, USA. E-mail: nmkidwell@wm.edu

† Electronic supplementary information (ESI) available. See DOI: https://doi.org/10.1039/d4cp02254h

multiphoton ionization spectroscopy to record the A–X vibronic transitions of NO–propane and NO–(*n*-butane).[8] From the vibronic spectra, they found the dissociation energies of the A and X electronic states to be $D_0' = 435\ \text{cm}^{-1}$ and $D_0'' = 245\ \text{cm}^{-1}$ for propane, and $D_0' = 435\ \text{cm}^{-1}$ and $D_0'' = 305\ \text{cm}^{-1}$ for *n*-butane. However, the complicated interactions and plausible isomer complexes contributing to the vibronic spectra of these weakly-bound systems made it challenging to interpret the experimental data.

Recently, this laboratory has carried out infrared spectroscopy and dynamics studies on NO–methane (CH_4) and NO–ethane complexes.[9,10] In the present work, we aim to investigate the spectroscopic and dynamical signatures from alkane chain elongation by characterizing NO–propane and NO–(*n*-butane), which have received relatively little attention. To this end, we compare the evolution of the vibrational predissociation dynamics between NO–CH_4 through NO–(*n*-butane) to gain deeper insights into the bimolecular collision outcomes on multidimensional potential energy surfaces. While NO–CH_4 and NO–ethane have a propensity to undergo prompt dissociation to NO + alkane products, the mechanisms that give rise to their respective observable outcomes are drastically different due to experiencing either Jahn–Teller or pseudo Jahn–Teller dynamics. Using a range of laser-based techniques, we analyze the infrared spectroscopy and infrared-driven dynamics of NO–propane and NO–(*n*-butane) to characterize the prompt and relatively slower predissociation pathways.

Methods

The spectroscopy and dynamics experiments investigating the bimolecular collision complexes between NO and alkanes (*e.g.*, NO–alkane; alkane = methane, ethane, propane, and butane) were carried out using a custom-built, high-vacuum apparatus. To generate cold NO–alkane complexes, a supersonic jet expansion was formed by pulsing a gas mixture containing NO, alkane and argon (Ar) into the source chamber. For NO–methane, a single gas flow channel was used containing 1% NO, 15% methane and Ar. The remaining NO–alkane experiments utilized a dual-flow nozzle consisting of two distinct gas flow channels that converged into a single gas line. One gas flow channel contained 1% NO/Ar, while the other contained 10% alkane/Ar (ethane, propane or butane). During all experiments, a total pressure of ∼5.5 bar was maintained, and the gas mixture was ejected through a 500 μm pulse valve nozzle (Series 9, General Valve) into the high-vacuum apparatus. Subsequently, NO–alkane molecular complexes were produced through adiabatic collisional cooling with the inert gas carrier, Ar. To isolate NO–alkane complexes with minimal internal energy from the molecular beam, a skimmer (ID: 2 mm, Beam Dynamics) positioned approximately 30 mm from the pulse valve nozzle was employed.

Downstream characterization of NO–alkane complexes was conducted using several laser-based methods. A Nd:YAG-pumped dye laser (Radiant Dyes, NarrowScan, 10 Hz) in conjunction with a series of BBO crystals generated ultraviolet (UV) radiation to detect NO fragments from the vibrational predissociation of cold, open-shell molecular complexes. Additionally, tunable IR radiation was produced using an optical parametric oscillator/amplifier (OPO/OPA, LaserVision) pumped by another Nd:YAG laser (Continuum Surelite II-10, 5 Hz). The spatially overlapped and counter-propagating IR and UV beams, both vertically polarized in the plane of the detector, intersected the molecular beam in the collision-free region in a perpendicular fashion following the skimmer.

IR action spectroscopy was performed to characterize the NO–alkane complex vibrational modes that are coupled to the reaction coordinate generating NO and alkane co-fragments. The IR pump laser prepared NO–alkane complexes with a single quantum of CH vibrational excitation, which exceeds the dissociation energy of the NO–alkane complex and leads to vibrational predissociation. To this end, the IR pump laser was scanned across the CH stretch region (2850–3050 cm^{-1}), while a UV probe laser was fixed on a rovibrational transition of NO ($X^2\Pi$, $v'' = 0$, J'', F_n, Λ) products generated from vibrational activation of the NO–alkane molecular complex. Using a wavelength meter (Coherent WaveMaster), the spin–orbit (F_1 and F_2) and Λ-doublet ($\Pi(A'')$ and $\Pi(A')$) levels were probed using the $Q_1(J'')$, $R_1(J'')$, $Q_2(J'')$, and $R_2(J'')$ rovibrational lines. As the IR pump laser became resonant with a NO–alkane transition in the CH stretch region, signal gain in the NO^+ mass ion channel was monitored and averaged with respect to the IR wavelength using active baseline subtraction.

Velocity map imaging (VMI) experiments, conducted under identical conditions, aimed to uncover the vibrational predissociation outcomes following IR activation of NO–alkane molecular complexes. Using the imaging mode of the spectrometer, the translational and angular distributions of NO ($X^2\Pi$, $v'' = 0$, J'', F_n, Λ) products were recorded from IR fragmentation of NO–alkanes. The IR activation wavelengths were chosen from the identified NO–alkane transitions in their respective IR action spectrum. The NO^+ ions were accelerated on axis with the molecular beam using a stack of ion optic plates and velocity-focused onto a position-sensitive multichannel plate/phosphor screen detector that was gated for the NO^+ mass ($m/z = 30$). Ion images were acquired using a charge-coupled device (CCD) camera, with 3D ion image reconstruction facilitated by the pBASEX program,[11] which was also used to determine the anisotropy parameter β across the main features in the ion images. The velocity distributions of NO ($X^2\Pi$, $v'' = 0$, J'', F_n, Λ) fragments were obtained using pBASEX by applying an inverse Abel transformation along the vertical axis and integrating the radial distributions over the polar angle. From conservation of momentum, the total kinetic energy release (TKER) distributions to NO + alkane products were obtained.

NO product state distributions were determined by scanning the UV probe through different NO A–X (0,0) transitions, while the IR pump laser remained fixed on a NO–alkane vibrational transition. Quantitative population analysis from product state distribution measurements was conducted by converting the relative transition intensities to relative populations using established procedures.[12,13] In particular, the monitored signal intensity was integrated and divided by the state degeneracy factor ($2J'' + 1$), probe pulse energy, and the line strength from LIFBASE[14] to obtain the population of the individual states. The intensity of the NO ($X^2\Pi$, $v'' = 0, J''$) signals was scaled relative to the $Q_1(J'' = 6.5)$ level signal, which was scanned before and after each probe line. During experiments, the gas pulse was interrogated near the leading edge to limit any contributions that may arise due to high-order complex formation beyond the NO–alkane bimolecular collision complex. Furthermore, the NO ($X^2\Pi$, $v'' = 0$, J'', F_n, Λ) rotational product state distributions and the ion image results were unchanged when heating the nozzle, indicating that high-order complex formation did not play a major role.

All calculations were performed using the Gaussian 16 suite.[15] We utilized the global minima as reported by Wright and co-workers[8] for NO–ethane, NO–propane, and NO–(*n*-butane) at the MP2/aug-cc-pVTZ level of theory. In addition, anharmonic vibrational frequency calculations were carried out for ethane, propane, and *n*-butane at the MP2/aug-cc-pVTZ level of theory.

Results and discussion

A. Infrared action spectroscopy in the CH stretching region

To characterize the vibrational spectroscopy of the NO–alkane collision complexes, infrared action spectroscopy was carried out to identify the transitions that induce vibrational predissociation of these weakly bound, open-shell systems. Shown in Fig. 1 are the IR action spectra for NO–methane (CH_4), NO–ethane, NO–propane and NO–(*n*-butane) in the region of the CH stretching vibrational modes over the ∼2850–3200 cm^{-1} range. Furthermore, illustrated in the right-hand side of the figure are the calculated global minima for the respective NO–alkane isomers reported by Wright and co-workers.[8] The non-covalent interaction isosurfaces are imprinted on the optimized geometries and were obtained using NCIPlot,[16] displaying the weak van der Waals interactions between NO with the alkane collision partner. In our previous work on NO–CH_4,[9] the broad IR feature was assigned to the asymmetric CH stretch, with a shoulder transition displaced by +30 cm^{-1} from the band origin and was assigned to the intermolecular bending mode. Likewise, we assigned the broadened band at ∼2996 cm^{-1} in the NO–ethane IR action spectrum to the in-phase asymmetric CH stretch ($\nu_7(\perp)$).[10] As can be observed in the figure, the homogenous linewidths of both transitions are significantly large, indicating that the vibrational predissociation lifetimes of the asymmetric CH stretch modes are short. Therefore, the asymmetric CH stretches are directly coupled to the intermolecular dissociation coordinate and induce prompt dissociation of each collision complex. In viewing the form of the asymmetric CH stretch vibrational modes of NO–CH_4 and NO–ethane, there is a simultaneous stretching of the facial hydrogen atoms closest to NO and a compression of the posterior hydrogen atoms of the alkane. The IR transitions for NO–ethane at 2900 cm^{-1} and 2933/2957 cm^{-1} were assigned to the out-of-phase symmetric CH stretch ($\nu_5(\parallel)$) and to the perpendicular and parallel $\nu_8 + \nu_{11}$ combination bands, respectively, involving asymmetric methyl deformation modes. Notably, the NO–ethane transitions at lower energy in the IR action spectrum display narrower linewidths, indicating that these modes lead to vibrational predissociation on a relatively slower timescale. Therefore, we concluded that the $\nu_5(\parallel)$ and $\nu_8 + \nu_{11}$ ($\perp$ and $\parallel$) modes are only moderately coupled to the reaction coordinate.

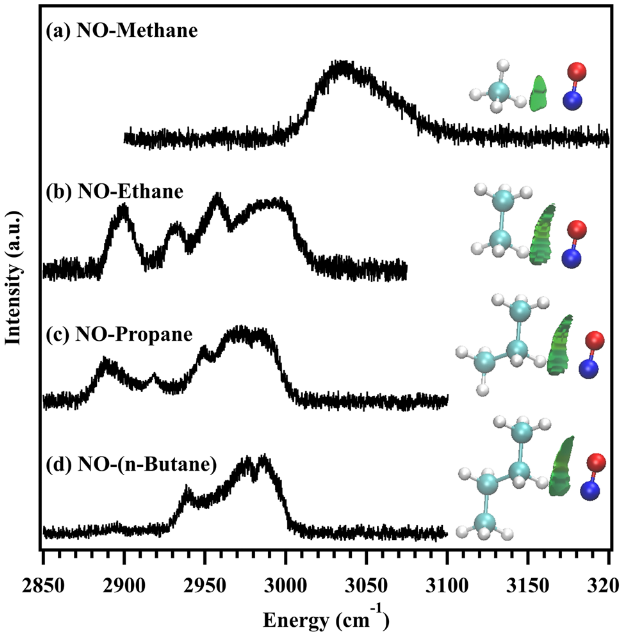

Fig. 1 Infrared action spectra for the series of NO–alkane collision complexes, (a) NO–methane, (b) NO–ethane, (c) NO–propane, and (d) NO–(*n*-butane). The global minimum for each complex is illustrated on the right-hand side, with the noncovalent interaction isosurfaces superimposed on the structures. The green isosurfaces indicate the increasing van der Waals interactions between NO and the growing alkane collision partner. The NO–CH_4 IR action spectrum is adapted with permission from Davis *et al.*, *J. Phys. Chem. A*, 2023, **127**, 5171.[9] Copyright 2023 American Chemical Society. The NO–ethane IR action spectrum is reproduced from ref. 10 with permission from the Royal Society of Chemistry.

Shown further below in Fig. 1, the IR action spectra of NO–propane and NO–(*n*-butane) were also recorded, featuring a similar array of transitions to NO–CH_4 and NO–ethane. With additional evidence given below, we tentatively classify the transition features at higher energy to the asymmetric CH stretches and the bands at lower energy to the symmetric CH modes. Here, we note that the intensity reduction in the symmetric CH stretch bands indicate their decreasing role in fragmenting the larger NO–propane and NO–(*n*-butane) collision complexes, plausibly caused by their diminishing coupling to the intermolecular bond dissociation coordinate. Simultaneously, the linewidths of the asymmetric CH stretch transitions also decrease as the alkane chain length lengthens, which suggests that the lifetime of the final vibrational quantum state increases. Activation of the asymmetric CH stretch modes of NO–propane and NO–(*n*-butane) may, therefore, preferentially

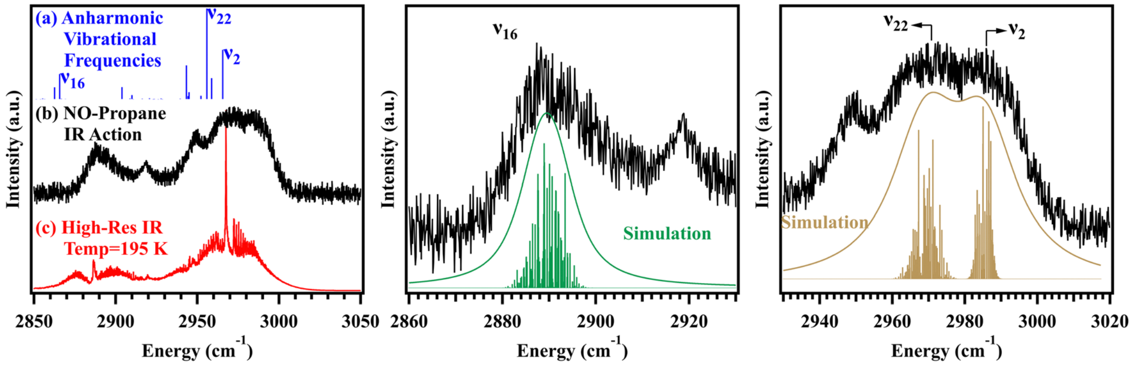

Fig. 2 (Left panel) Theoretical and experimental infrared spectra, showing the (a) calculated anharmonic vibrational frequencies of propane, (b) experimental IR action spectrum for the NO–propane collision complex, and (c) high-resolution IR absorption spectrum of propane recorded at 195 K, obtained from ref. 17. (middle and right panels) Close views of the ν_{16} and ν_{22}/ν_2 transition bands of NO–propane. The rovibrational simulations were obtained using the fitting procedure described in the main text and the spectroscopic constants listed in Table 1. The green and gold traces represent the fitted spectra by convoluting each stick with a Lorentzian line shape function.

result in a relatively slower dissociation mechanism compared to the favored prompt dissociation pathway of NO–CH_4 and NO–ethane when exciting analogous modes.

The left panel of Fig. 2 shows the IR action spectrum of NO–propane in excellent agreement with the calculated, anharmonic vibrational frequencies of propane (the IR chromophore) at the ωB97X-D/6-311+G(d,p) level of theory depicted as blue sticks. The IR action spectrum of NO–propane also agrees well with the high-resolution IR absorption spectrum of propane (shown as the red trace) recorded at 195 K by Sharpe *et al.* obtained *via* HITRAN.[17] In agreement with the assignments made in the previous paragraph, the transition at 2888 cm^{-1} in the NO–propane IR action spectrum best coincides with the calculated out-of-phase symmetric CH stretch (ν_{16} (b_1)). Furthermore, this assignment for NO–propane is strengthened by the fact that the lowest vibrational band of NO–ethane was also assigned to the out-of-phase symmetric CH stretch. Additionally, the vibrational transitions at 2919 and 2949 cm^{-1} in the IR action spectrum of NO–propane are likely due to combination bands involving methyl deformation modes. Lastly, the broad feature at higher energy is tentatively assigned to the asymmetric CH stretch, similar to NO–ethane. We now turn to the rovibrational simulations for the symmetric and asymmetric CH stretches.

pGOPHER[18] was utilized to carry out the rovibrational simulations for the experimental ν_{16} (b_1) band contour of NO–propane, in which propane was treated as an asymmetric top molecule in the C_{2v} point group. In the middle panel of Fig. 2, the experimental ν_{16} feature in the IR action spectrum is compared to the rovibrational simulation results shown in green, which were determined using the optimized spectroscopic constants[19] listed in Table 1. To obtain the best fit to the experimental results, the ν_{16} feature with b_1 symmetry in the C_{2v} point group was simulated as the out-of-phase symmetric CH stretch of NO–propane. The green sticks portray the simulated rovibrational transitions of the complex, while a Lorentzian line shape function ($\Delta\nu_{\mathrm{Lor}}$) was included in the fitting procedure to best match with the homogeneous linewidth of the ν_{16} transition. An upper limit of approximately 9 cm^{-1} full width at half maximum was found for the homogenous broadening, which correlates to a vibrational predissociation lifetime of τ_{vib} = 590 fs.

Table 1 Spectral fitting parameters obtained for the NO–propane rovibrational simulations[a]

	ν_{16} (b_1)	ν_{22} (b_2)	ν_2 (a_1)
Parameter[b]	Value	Value	Value
ν_0	2888.3(3)	2968.1(3)	2985.2(3)
A''/A'	0.974(1)[c]	0.974(1)[c]	0.974(1)[c]
B''/B'	0.282(1)[c]	0.282(1)[c]	0.282(1)[c]
C''/C'	0.249(1)[c]	0.249(1)[c]	0.249(1)[c]
$D_{J''}$	2.40×10^{-7}(1)	2.40×10^{-7}(1)	2.40×10^{-7}(1)
$D_{J''K''}$	8.99×10^{-7}(1)	8.99×10^{-7}(1)	8.99×10^{-7}(1)
$D_{K''}$	5.33×10^{-6}(1)	5.33×10^{-6}(1)	5.33×10^{-6}(1)
$\Delta\nu_{\mathrm{Lor}}$	9(1)	20(1)	20(1)
T_{rot} (K)	4(1)	4(1)	4(1)

[a] Standard deviations (2σ) for each parameter are given in parentheses. [b] Otherwise indicated, all values are given in wavenumbers (cm^{-1}). [c] Ref. 19.

The right-hand panel of Fig. 2 displays a closer view of the NO–propane IR action spectrum from ~2930–3020 cm^{-1} and presents the spectral fitting results for the asymmetric CH stretch region of NO–propane. Upon inspection of this rather broad spectral feature at higher energy, it is more clearly visible that two vibrational bands likely comprise the band envelope. Informed from the anharmonic frequency calculations, we attribute the lower-energy component at 2968 cm^{-1} to the ν_{22} (b_2) asymmetric CH stretch mode, involving in-phase CH_2 nuclear displacement. Furthermore, the higher-energy component of the band envelope at 2985 cm^{-1} is assigned to the in-phase asymmetric CH stretch (ν_2 (a_1)). Indeed, the form of the ν_2 (a_1) mode resembles the same in-phase asymmetric CH stretch vibrations of NO–CH_4 and NO–ethane, with simultaneous stretching of the facial hydrogen atoms relative to NO and a compression of the posterior hydrogen atoms. The rovibrational simulated results are represented with gold sticks for the respective vibrational band components and the gold

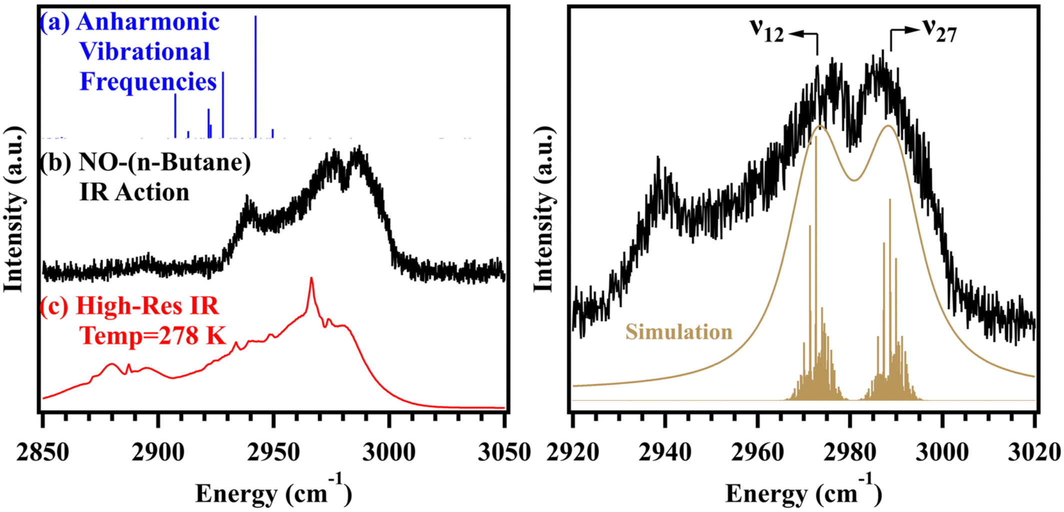

Fig. 3 (Left panel) Theoretical and experimental infrared spectra, showing the (a) calculated anharmonic vibrational frequencies of *n*-butane, (b) experimental IR action spectrum for the NO–(*n*-butane) collision complex, and (c) high-resolution IR absorption spectrum of *n*-butane recorded at 278 K, obtained from ref. 17. (Right panel) Close view of the ν_{12}/ν_{27} transition bands of NO–(*n*-butane). The rovibrational simulations were obtained using the fitting procedure described in the main text and the spectroscopic constants listed in Table 2. The gold trace represents the fitted spectrum by convoluting each stick with a Lorentzian line shape function.

trace is the result of incorporating a $\sim$20 cm^{-1} homogeneous broadening in the fit procedure for best agreement with experiment, indicating that the vibrational predissociation lifetime is approximately τ_{vib} = 265 fs. In light of the spectral fitting results for NO–propane, we revisited the spectroscopic assignments in the asymmetric CH stretch region for NO–ethane, and we determined that two components were also contained within the broad transition feature as opposed to a single band. These results are placed in the ESI.†

Increasing the alkane collision partner chain length, Fig. 3 shows the calculated and experimental IR results for NO–(*n*-butane). In particular, the top blue sticks in the left panel of Fig. 3 show the anharmonic frequency results for *n*-butane as the spectral carrier at the ωB97X-D/6-311+G(d,p) level of theory. Just below the theoretical frequency predications, the IR action spectrum of NO–(*n*-butane) is in excellent agreement with the calculated results. Whereas the symmetric CH stretch transitions were observable in the NO–ethane and NO–propane IR action spectra, these transitions for NO–(*n*-butane) are comparatively much weaker, although the IR absorption spectrum of *n*-butane at 278 K (red trace) reveals a weak transition plausibly due to the symmetric CH stretch. Therefore, we conclude that the symmetric CH stretch transitions do not play a significant role in fragmenting the NO–(*n*-butane) collision complex, leading to their weak transition intensity in the IR action spectrum. However, the band at 2938 cm^{-1} is still visible in the spectrum, and with support from calculations and the previous mode assignments for NO–ethane and NO–propane, this feature is attributed to a combination band involving methyl deformation with CH_2 scissoring modes.

At higher energy in the IR action spectrum, and shown with a closer view in the right panel of Fig. 3, are two noticeable transition bands that are more distinct compared to the smaller NO–alkane collision complexes at the same IR wavelength. We assign the transition peak at 2972 cm^{-1} to the asymmetric CH stretch mode that predominantly exhibits in-phase CH_2 bond distortions, namely the ν_{12} (a_u) mode. Furthermore, at 2988 cm^{-1}, the vibrational band feature is assigned to the ν_{27} (b_u) mode, which is characterized as the in-phase asymmetric CH stretch where the hydrogen atoms nearest the NO partner stretch and the posterior hydrogen atoms contract concurrently. When carrying out the rovibrational simulations for NO–(*n*-butane) in a similar manner as NO–propane, the *n*-butane chromophore was under the C_{2h} point group. The gold sticks in Fig. 3 represent the rovibrational simulations with the spectroscopic constants[20] given in Table 2 and the gold trace was generated with a $\Delta\nu_{\text{Lor}}$ = 13 cm^{-1} convolution for overall good agreement with the experimental IR action spectrum. In increasing alkane chain length, the vibrational predissociation lifetime of the in-phase asymmetric CH stretch is τ_{vib} = 170 fs, 210 fs, 265 fs, and 410 fs for NO–CH_4, NO–ethane, NO–propane, and NO–(*n*-butane), respectively. Therefore, it is anticipated that prompt dissociation dynamics will generate NO + alkane

Table 2 Spectral fitting parameters obtained for the NO–(*n*-butane) rovibrational simulations[a]

	ν_{12} (a_u)	ν_{27} (b_u)
Parameter[b]	Value	Value
ν_0	2972.1(3)	2988.3(3)
A''/A'	0.7742(1)/0.7734(1)[c]	0.7742(1)/0.7736(1)[c]
B''/B'	0.1199(1)/0.1200(1)[c]	0.1199(1)/0.1199(1)[c]
C''/C'	0.1127(1)/0.1127(1)[c]	0.1127(1)/0.1126(1)[c]
$\Delta\nu_{\text{Lor}}$	13(1)	13(1)
T_{rot} (K)	4(1)	4(1)

[a] Standard deviations (2σ) for each parameter are given in parentheses. [b] Otherwise indicated, all values are given in wavenumbers (cm^{-1}).

products, but since a subset of IR transition features decrease in intensity and others decrease in their spectral linewidth, we expect similar, albeit somewhat differing dynamics for NO–propane and NO–(*n*-butane) relative to NO–CH_4 and NO–ethane. We now turn the section to focus on the IR activation dynamics of NO–propane and NO–(*n*-butane) to reveal their inelastic scattering mechanisms, towards developing a deeper understanding of the dynamics related to NO–CH_4 and NO–ethane.

B. Dynamics of infrared-activated collision complexes

The relative energies and impact configurations of collision partners drive the extent to which mechanistically different pathways are sampled for reactive and nonreactive systems. Starting from a similar initial isomer geometry (see Fig. 1), preparing the NO–alkane collision complexes with vibrational mode specificity yields insights into the dynamical signatures from fragmentation as the alkane chain length increases. As Fig. 1 shows, the asymmetric CH stretch is a shared transition feature in each of the NO–alkane IR action spectra, with broad linewidths signifying fast vibrational predissociation lifetimes and thus prompt dynamics. However, as discussed in the previous section, there is a systematic decrease in the relative transition breadths for the asymmetric CH stretch bands from NO–CH_4 to NO–(*n*-butane). When activating the NO–alkane collision complexes with their respective asymmetric CH stretch vibrational mode, we recorded the velocity map ion images (VMI) and product state distributions of NO ($X^2\Pi$, $v'' = 0$, J'', F_n, Λ) fragments to report on the degree to which prompt and slow fragmentation occurs. The dynamical signatures are encoded in the ion image anisotropy and total kinetic energy release (TKER) distributions, in addition to the relative populations in the NO ($X^2\Pi$, $v'' = 0$, J'', F_n, Λ) product quantum states.

Shown as insets in Fig. 4 and 5 are the ion images recorded for specific NO ($X^2\Pi$, $v'' = 0$, J'', F_n, Λ) product states from IR excitation of the asymmetric CH stretch for NO–propane and NO–(*n*-butane), respectively. During experiments, the IR excitation laser is vertically polarized relative to the detector plane. As illustrated in the figures, the degree of image anisotropy is sensitive to the probed NO rotational level. For example, the ion images monitoring the lower $F_1(^2\Pi_{1/2})$ spin–orbit state ($Q_1(J'')$ and $R_1(J'')$ levels) with modest rotational energy appear anisotropic, whereas the ion images are isotropic when detecting large J'' levels in the lower $F_1(^2\Pi_{1/2})$ spin–orbit state and all J'' levels in the upper $F_2(^2\Pi_{3/2})$ spin–orbit state. More specifically, only the $Q_1(J'' = 5.5\text{–}10.5)$ and $R_1(J'' = 2.5\text{–}4.5)$ levels are anisotropic for both NO–propane and NO–(*n*-butane). The angular distribution can be extracted quantitatively from ion images by converting the laboratory frame to the molecular frame distribution using the equation, $I(\theta) = (1 + \beta \times P_2(\cos\theta))/4\pi$. In this expression, θ is the angle between the fragment velocity vector and the vertical laser polarization, and P_2 is a second-order Legendre polynomial. The anisotropy parameter β yields information on the angular distribution of NO products in the ion image. Following analysis using pBASEX, β for the anisotropic image in Fig. 4 is $\sim$+0.33(3) and $\sim$+0.25(4) in Fig. 5 on average, which verifies the ion images are anisotropic. This is consistent with NO–propane and NO–(*n*-butane) undergoing prompt dissociation on a timescale that is faster compared to their rotational periods based on calculated rotational constants; τ_{rot}(NO–propane) $\sim$5.6 ps and τ_{rot}(NO–(*n*-butane) $\sim$7.9 ps). The TKER distributions for NO + propane or *n*-butane co-products are displayed alongside the ion images as black traces. When probing NO ($Q_1(6.5)$) products from NO–propane IR-induced decay in Fig. 4, the prominent feature in the TKER distribution peaks at approximately 325 cm^{-1} with a full-width at half maximum of $\sim$560 cm^{-1}. Additionally, when IR activating NO–(*n*-butane), the main feature in the TKER distribution for NO ($R_1(4.5)$) products in Fig. 5 is located at 290 cm^{-1} and has a breadth of 550 cm^{-1}. Furthermore, $\beta \sim 0$ on average for the ion images appearing isotropic, and the main feature in their respective TKER distributions appear at $\sim$250 cm^{-1} and have breadths of $\sim$480 cm^{-1}. Therefore, for both NO–propane and NO–(*n*-butane), a subset of NO products is generated from a prompt dissociation pathway following IR activation of the asymmetric CH stretch modes, while for another subset of NO products, a different mechanism takes place characterized by slower vibrational predissociation dynamics. The ion image anisotropy results are similar to NO–ethane,[10] in which a narrow distribution of rotational levels in the lower $F_1(^2\Pi_{1/2})$ spin–orbit state exhibited anisotropic images. However, the ion images recorded from NO–CH_4 dissociation[9] displayed anisotropic ion images for both spin–orbit states of NO products. We now turn the discussion to focus on the NO ($X^2\Pi$, $v'' = 0$, J'', F_n, Λ) product state distributions from vibrational predissociation of NO–CH_4 through NO–(*n*-butane) to quantify the population of products generated from either the prompt or slow predissociation mechanisms.

C. Dissociation dynamics of vibrationally excited of NO–alkanes

The two ground electronic states of the NO radical are formed as a result of the angular momentum coupling between the electron spin and the π* molecular orbital in which the lone electron resides.[21] Consequently, the NO spin–orbit states $F_1(^2\Pi_{1/2})$ and $F_2(^2\Pi_{3/2})$ are separated by 119.82 cm^{-1}. Crespo-Otero[22] determined the ground state potential energy surfaces of NO–CH_4 that were constructed from different NO and CH_4 monomer orientations. These Jahn–Teller surfaces are defined by the relative orientation of the π* molecular orbital of NO in relation to the plane of symmetry as either monomer undergoes rotation. For the lowest-energy isomer of NO–CH_4, the two Jahn–Teller surfaces intersect at the C_{3v} geometry, resembling an NO–H_3C–H structure. Upon a Jahn–Teller rotation, a lower energy and reduced C_s symmetry configuration is obtained, wherein the N═O bond is perpendicular to the facial hydrogen atoms of CH_4. Correspondingly, the upper and lower Jahn–Teller surfaces have A' and A'' symmetry, respectively.

In generating the NO–CH_4 collision complex, the upper (A') and lower (A'') Jahn–Teller surfaces are energetically separated by a spin–orbit splitting ($a\zeta_e d$) factor due to a combination of electronic and vibronic quenching.[23] This energy separation (ΔE) for open-shell complexes can be determined using the

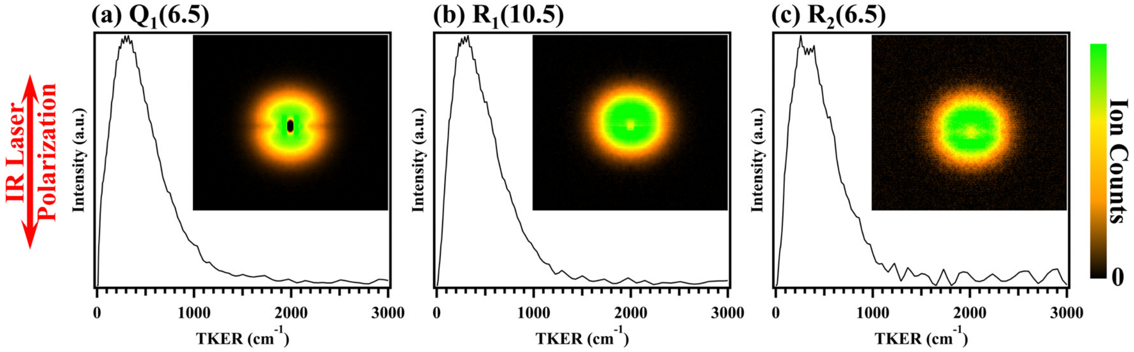

Fig. 4 Total kinetic energy release (TKER) distributions of propane and (a) NO $Q_1(J'' = 6.5)$, (b) NO $R_1(J'' = 10.5)$, or (c) NO $R_2(J'' = 6.5)$ products from IR activation of NO–propane complexes. The insets show the experimental ion images, revealing the angular distributions. The IR pump laser is parallel to the detector plane and the ion count range is displayed on the right.

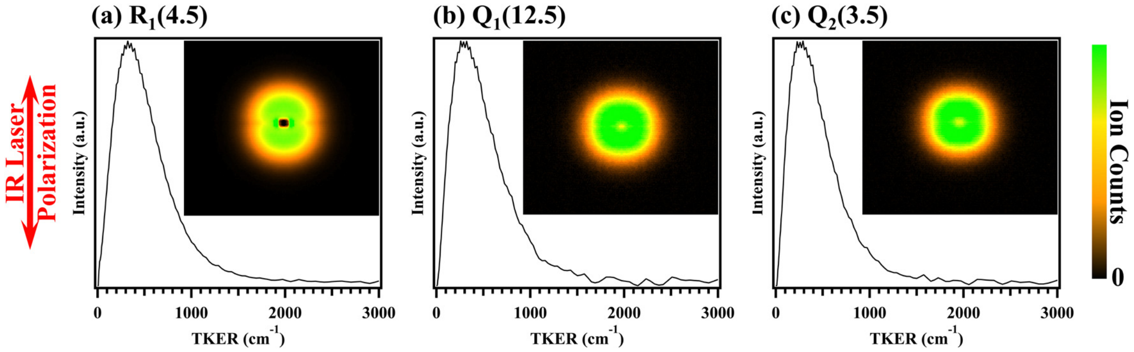

Fig. 5 Total kinetic energy release (TKER) distributions of *n*-butane and (a) NO $R_1(J'' = 4.5)$, (b) NO $Q_1(J'' = 12.5)$, or (c) NO $Q_2(J'' = 3.5)$ products from IR activation of NO–(*n*-butane) complexes. The insets show the experimental ion images, revealing the angular distributions. The IR pump laser is parallel to the detector plane and the ion count range is displayed on the right.

formula, $\Delta E = \sqrt{\left[(\Delta E_0)^2 + (a\zeta_e d)^2\right]}$, where ΔE_0 is the Jahn–Teller splitting of NO–CH_4. In our previous work,[9] $a\zeta_e d$ for NO–CH_4 was determined to have an upper limit of 120 cm^{-1}. With the ΔE_0 = 30 cm^{-1} Jahn–Teller splitting calculated by Crespo-Otero,[22] ΔE for NO–CH_4 is predicted to be between 104–124 cm^{-1}. Since the zero-point energy of NO–CH_4 is close to ΔE,[22] it is possible that NO–CH_4 complexes generated with rotational internal energy may interconvert between the A' and A'' Jahn–Teller surfaces. Previously,[9] we interpreted the spectroscopic and dynamical signatures from NO–CH_4 fragmentation to result from four main mechanisms. In particular, IR activation of four distinct NO–CH_4 population subsets may take place, wherein vibrational predissociation occurs directly from the A' or A'' Jahn–Teller surfaces or following $A' \leftrightarrow A''$ interconversion. Therefore, the anisotropic images that appeared for a narrow distribution of NO ($X^2\Pi$, $v'' = 0, J'', F_n, \Lambda$) product states were assigned to the Jahn–Teller dynamics prior to IR activation of NO–CH_4. To validate our hypothesis, both energy and symmetry conservation between NO–CH_4 complexes and the NO ($X^2\Pi$, $v'' = 0, J'', F_n, \Lambda$) + CH_4 (ν) product states were confirmed. Upon IR excitation of the asymmetric CH stretch mode of NO–CH_4, vibration-to-vibration energy transfer to the umbrella acceptor mode of CH_4 products was determined to the dominant mechanism characteristic of prompt vibrational predissociation.

Increasing the alkane chain length results in a greater interaction strength due to the polarizability between NO and the alkane collision partner. Therefore, this lifts the near-degeneracy at the high-symmetry intersection for NO–CH_4 to form two pseudo Jahn–Teller surfaces for larger NO–alkanes. A similar calculation for the energy splitting of the two pseudo Jahn–Teller states of NO–ethane was carried out,[10] resulting in an upper limit of ΔE ~178–211 cm^{-1}. This energy separation between the two pseudo Jahn–Teller states, in combination with an anticipated decrease in the zero-point energy levels of NO–ethane, may conceivably turn off the interconversion mechanism and therefore limit population from accessing the other pseudo Jahn–Teller surface. The dynamical signatures arising from prompt NO–ethane decay were imprinted on the NO ($X^2\Pi$, $v'' = 0, J'', F_n, \Lambda$) ion images as anisotropic angular distributions, now only appearing in the lower $F_1(^2\Pi_{1/2})$ state for a limited range of low J'' levels. Thus, the anisotropic ion images for certain NO $Q_1(J'')$ and $R_1(J'')$ product levels were assigned to prompt NO–ethane vibrational predissociation from the upper and lower pseudo Jahn–Teller states.

In similar fashion, an upper limit calculation of ΔE for the NO–propane and NO–(*n*-butane) pseudo Jahn–Teller states is

$\sim$256–304 cm^{-1} and $\sim$330–391 cm^{-1}, respectively, when approximating ΔE_0 and $a\zeta_e d$ using the relative polarizability of propane and *n*-butane. Notably, the energy separation between the pseudo Jahn–Teller states is becoming larger with the alkane size, while the zero-point energy levels are simultaneously decreasing in energy. As discussed for NO–ethane, the population distribution for NO–propane and NO–(*n*-butane) will likely reside in either of the two pseudo Jahn–Teller surfaces without the ability to transfer to its conjugate state. With the population interconversion mechanisms not accessible, IR activation will plausibly only take place for the two population subsets occupying the pseudo Jahn–Teller surfaces without the interconversion dynamics present. Therefore, the prompt vibrational predissociation dynamics of NO–propane and NO–(*n*-butane) are projected to be similar to NO–ethane.

In the analysis that follows, an analogous discussion can also be extended to NO–(*n*-butane), but here we will focus on the NO–propane dissociation mechanisms and outcomes. Fig. 1 shows the global minimum geometries for NO–CH_4 through NO–(*n*-butane), which share the common configuration with NO perpendicularly oriented to the three facial hydrogen atoms of the alkane. A reduction in symmetry and energy *via* a Jahn–Teller active mode such as intermolecular rotation will result in NO–propane adopting a non-symmetric geometry. Depending on the NO π* molecular orbital's orientation with respect to the plane of symmetry, the two pseudo-Jahn–Teller surfaces are generated, as discussed above for NO–ethane. An energy-level diagram illustrating the inelastic scattering dynamics of NO–propane collision complexes is shown in Fig. 6, however, without the pseudo Jahn–Teller surfaces displayed. As shown in the right-hand side of the figure, vibrational predissociation of NO–propane results in populating the internal energies (vibrational, rotational, spin–orbit) of NO ($X^2\Pi$, $\nu'' = 0, J'', F_n, \Lambda$) and propane, in addition to the relative recoil velocity (TKER) between the products. Relative to the NO–propane and NO–(*n*-butane) complexes, the NO + alkane asymptotic limits are $D_0'' = 245\ cm^{-1}$ and $305\ cm^{-1}$, respectively.[8]

According to the energy gap law,[24,25] when exciting the ν_2 asymmetric CH stretch of NO–propane, vibration-to-vibration energy transfer is most efficient for 'bright' acceptor modes of propane products that are near-resonant with and resemble the activated mode of the complex. With most of the available energy partitioned into propane vibration, the remaining energy may then be placed in the rotational manifolds within the $^2\Pi_{1/2}$ and $^2\Pi_{3/2}$ spin–orbit electronic states of NO. Relative to the asymptotic limit, Fig. 6 shows the internal vibrational energy of propane products increasing from bottom to top, while the internal rotational energy of NO ($\nu'' = 0$, $^2\Pi_{1/2}$ and $^2\Pi_{3/2}$) increases from top to bottom with respect to the available energy limit (grey line). The vibrational levels of propane were obtained from anharmonic calculations, depicting many propane acceptor mode candidates that may be populated following decay of NO–propane complexes. However, as previously determined for NO–CH_4 and NO–ethane,[9,10] the 'bright' acceptor alkane modes are highly specific, with combination bands involving an umbrella mode of the three facial hydrogen atoms initially complexed to NO and a buckling mode. We tentatively assign the same mechanistic pathways available for prompt vibrational predissociation of NO–ethane to both NO–propane and NO–(*n*-butane). Highlighted as red lines in the propane vibrational levels, the $\nu_7 + \nu_4$ combination band at 2614 cm^{-1} involves nuclear motion resembling the umbrella and buckling modes. Here, the ν_4 umbrella mode of propane products has a similar form to the NO–propane ν_2 asymmetric CH stretch. With the available energy E_{avl} = 2723 cm^{-1}, determined from the IR photon energy ($E_{h\nu}$ = 2968 cm^{-1}) and dissociation energy ($D_0'' = 245\ cm^{-1}$), the additional energy is then stored in the rotational and/or translational degrees of freedom. However, in the experiment, we may be simultaneously activating the overlapping ν_{22} mode (in-phase asymmetric CH_2 stretch), possibly leading to occupying the methyl-wagging $\nu_{26} + \nu_{24}$ combination band of propane at 2639 cm^{-1}. By conservation of energy, the main features in the TKER distributions agree well with the $\nu_7 + \nu_4$ and $\nu_{26} + \nu_{24}$ vibrational levels of propane when detecting NO products. Furthermore, the NO ($X^2\Pi$, $\nu'' = 0, J'', F_n, \Lambda$) products with anisotropic ion images are also highlighted with red lines in the figure, indicating their formation from prompt NO–propane dissociation. Although there is a large density of 'dark' propane acceptor levels, the prompt vibrational predissociation mechanism of NO–propane (and, by extension, NO–(*n*-butane)) is selective, similar to NO–CH_4 and NO–ethane.

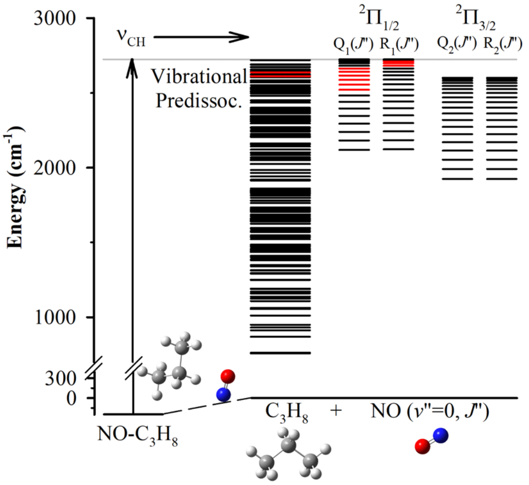

Fig. 6 Energy-level diagram, showing the inelastic scattering dynamics of NO–propane collision complexes. The NO–propane complexes are activated with the in-phase asymmetric CH stretch mode, indicated by the vertical black arrow, and initiates vibrational predissociation of NO–propane to NO ($X^2\Pi$, $\nu'' = 0, J'', F_n, \Lambda$) + propane ($\nu$) co-products. The energetically accessible vibrational states of propane fragments are shown, with increasing energy going up from the asymptotic limit. The allowed spin–orbit ($^2\Pi_{1/2}$, $^2\Pi_{3/2}$) and rotational levels (J'') of NO ($\nu'' = 0$) products are also shown following vibrational predissociation of NO–propane, with increasing energy going down from the available energy (grey line). The red-highlighted vibrational levels of propane are the likely 'bright' acceptor modes populated following fragmentation of NO–propane. The red NO ($X^2\Pi$, $\nu'' = 0, J'', F_n, \Lambda$) product levels indicate the probed states with ion images primarily displaying anisotropic angular distributions.

As the alkane chain length is elongated, the preference for the prompt *versus* the slow predissociation pathway is evident

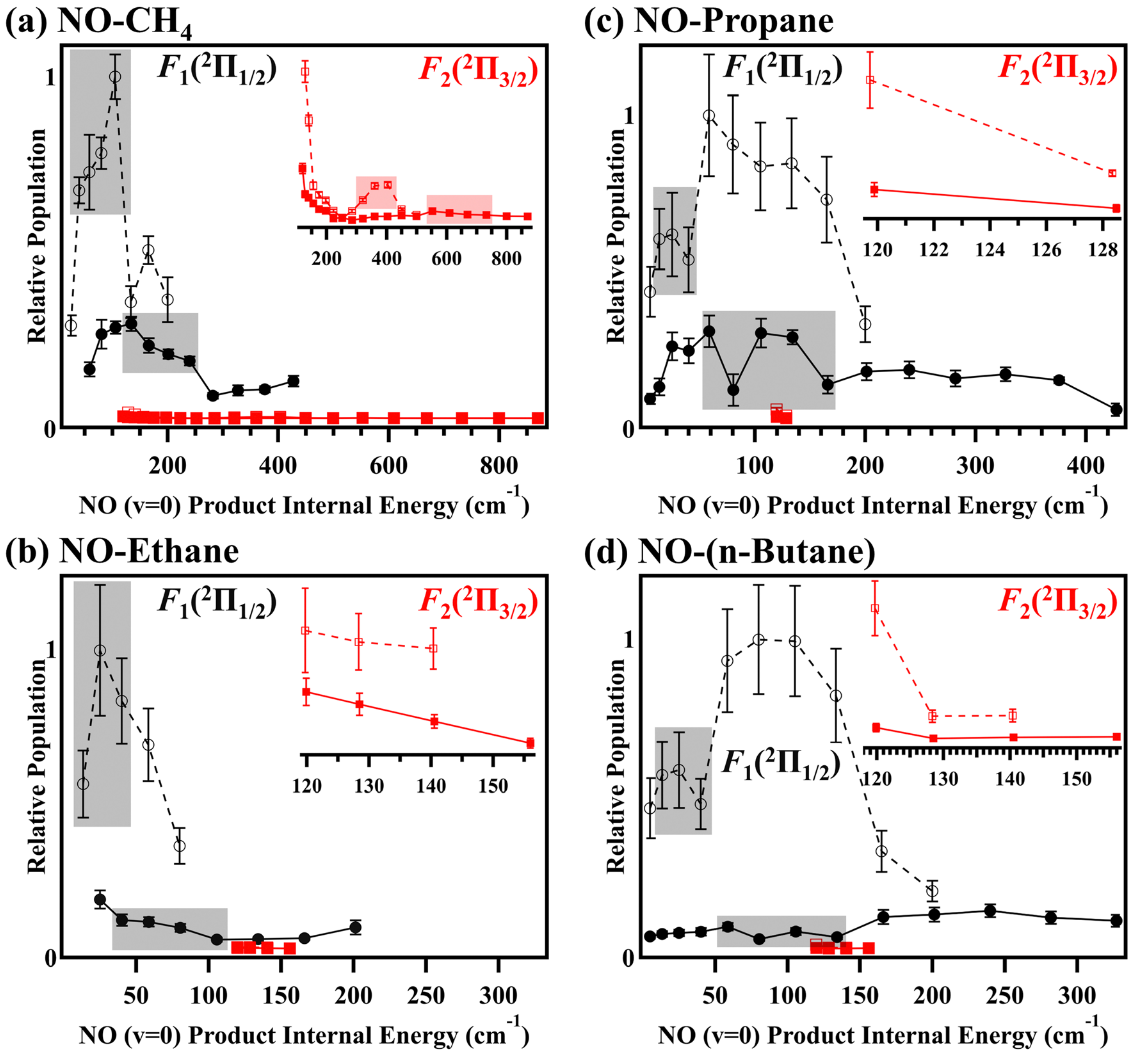

Fig. 7 Relative population in NO ($\nu'' = 0$) product rotational levels following infrared activation of (a) NO–CH$_4$, (b) NO–ethane, (c) NO–propane, and (d) NO–(*n*-butane) collision complexes. The population distribution is plotted with respect to the rotational and spin–orbit energy of NO products. The black traces identify the population in the lower $F_1(^2\Pi_{1/2})$ spin–orbit manifold, while the red traces report the populations in the upper $F_2(^2\Pi_{3/2})$ spin–orbit manifold. The insets show a closer view of the upper $F_2(^2\Pi_{3/2})$ spin–orbit distribution. The markers signify the Λ-doublet ($\Pi(A'')$ and $\Pi(A')$) components of NO, with the filled markers indicating the Q-branches ($\Pi(A'')$) and the open markers specifying the R-branches ($\Pi(A')$). Regions with rectangular shading indicate the NO ($X^2\Pi$, $\nu'' = 0$, J'', F_n, Λ) products displaying anisotropic ion images from fragmentation of their respective NO–alkane collision complex. From IR activation of the asymmetric CH stretch vibrational mode, the relative populations show that NO–CH$_4$ and NO–ethane fragment preferentially through prompt vibrational predissociation, while NO–propane and NO–(*n*-butane) favor a vibrational predissociation pathway on a comparatively slower timescale.

in the product state distribution results presented in Fig. 7. In particular, the figure shows the relative NO ($X^2\Pi$, $\nu'' = 0$, J'', F_n, Λ) product populations following IR activation of the NO–alkane collision complexes using the asymmetric CH stretch vibrational mode. The black and red traces show the $F_1(^2\Pi_{1/2})$ and $F_2(^2\Pi_{3/2})$ spin–orbit state populations, respectively; a closer view of the upper $F_2(^2\Pi_{3/2})$ state distribution is presented in the inset. Furthermore, the Q-branches (filled markers) are selective for the $\Pi(A'')$ Λ-doublet component, while $\Pi(A')$ is probed using the R-branch transitions (open markers).[26] Indeed, for all NO–alkanes, the results indicate that NO products are formed primarily in the lower $F_1(^2\Pi_{1/2})$ spin–orbit state, with a greater propensity to occupy the $\Pi(A')$ Λ-doublet manifold in both spin–orbit states. Following fragmentation of the NO–alkane collision complexes, the NO ($X^2\Pi$, $\nu'' = 0$, J'', F_n, Λ) products are thus generated with a strong electron-spin polarization, consistent with the larger $F_1(^2\Pi_{1/2})$ spin–orbit state population observed. Additionally, the product state distributions point to a Λ-doublet propensity for the $\Pi(A')$ state, signifying that the π* molecular orbital of NO products is aligned parallel to nuclear rotation. It is noteworthy that the interaction energy is smaller for all NO–alkane collision complexes when the π* molecular orbital of the NO partner is oriented towards the alkane,[8,22] which may give rise to the observed Λ-doublet population distribution.

The probed NO rotational levels in Fig. 7 that showed anisotropic ion images due to prompt fragmentation are highlighted with rectangular shading for each spin–orbit state.

As can be seen in the figure, the NO ($X^2\Pi$, $v'' = 0, J'', F_n, \Lambda$) product state distributions from NO–CH_4 and NO–ethane predissociation show that much of the NO population resides in the grey-highlighted regions, therefore indicating that the prompt dissociation pathway is their dominant decay mechanism. Furthermore, for the upper $F_2(^2\Pi_{3/2})$ spin–orbit state distribution of NO products from NO–CH_4 fragmentation, the population is relatively greater for the red-shaded NO J'' levels also displaying anisotropic images ascribed to Jahn–Teller dynamics. However, Fig. 7 also reveals that without population interconversion, the larger NO–alkanes are restricted to pseudo Jahn–Teller dynamics prior to IR activation since anisotropic ion images were only detected for the lower NO $F_1(^2\Pi_{1/2})$ spin–orbit state.

While prompt predissociation is still a moderately accessible pathway for NO–propane and NO–(n-butane) based on their relative population distributions, Fig. 7 also suggests that the slow predissociation pathway is increasingly preferred as the alkane chain length grows. Generally, the unshaded NO ($X^2\Pi$, $v'' = 0, J'', F_n, \Lambda$) product levels from NO–propane and NO–(n-butane) fragmentation having isotropic ion images are significantly more populated than their shaded counterparts. We attribute this qualitatively to the plausible restricted mobility of the NO and propane/butane monomers within the collision complexes. During IR activation of the lowest-energy isomer geometries of NO–propane and NO–(n-butane) shown in Fig. 1, internal rotation may occur such that the NO partner may explore another site on the propane or n-butane backbone. Consequently, the two monomers may become trapped in another isomer configuration, leading to predissociation on a slower timescale. However, it cannot be completely ruled out that another NO–propane or NO–(n-butane) isomer may be present during experiments that dissociates comparatively slower. Wright and co-workers report an increasing number of NO–alkane isomers as the alkane size increases, with barriers between them likely decreasing. If another NO–propane or NO–(n-butane) isomer were populated other than the configurations shown in Fig. 1, the slower dynamical signatures may be imprinted as isotropic ion images in the results. In the IR action spectra given in Fig. 2, the lower-energy component of the broad asymmetric CH stretch band was attributed to nuclear motion involving in-phase CH_2 displacement. Furthermore, this spectral feature became more resolved from NO–propane to NO–(n-butane), possibly indicating vibrational predissociation from a geometry where NO is interacting with the alkane backbone. Following fragmentation, the impulse generated from NO departing the alkane backbone would generate the greatest distortion along the CH_2 bonds yielding the observed transition band. Nevertheless, from a bimolecular collision standpoint, the relative impact orientations of the two NO and propane or n-butane collision partners will statistically sample many more geometries not conducive to prompt decay or efficient energy transfer. Rather, it is more probable that collisions will take place along the growing alkane chain backbone, resulting in energy exchange with a greater distribution of product internal energies.

A consistent, physical picture emerges for the NO–alkane collision complexes, wherein either Jahn–Teller or pseudo Jahn–Teller dynamics lead to the observed product outcomes. With increasing alkane size, the energy splitting between the Jahn–Teller surfaces also becomes larger. For NO–CH_4, the two potential energy surfaces form a conical intersection at a nearly-degenerate point, while an avoided crossing is generated for the larger NO–alkanes. Subotnik and co-workers[27,28] have demonstrated that the chemical dynamics and therefore the chemical reaction rates can be drastically impacted in such regions of strong, nonadiabatic coupling. In particular, the dynamic (pseudo) Jahn–Teller NO–alkane systems may encircle the region formed by the conical intersection or avoided crossing, and in doing so, may be influenced by a geometric (or 'Berry') phase. The geometric phase curvature can serve as an effective magnetic field on the electron spin,[27,29] which can cause an electron-spin dependence on the molecular dynamics and kinetic rates. As observed in the NO ($X^2\Pi$, $v'' = 0, J'', F_n, \Lambda$) product state distribution results, there is a strong electron spin polarization, in which the lower spin–orbit state is preferentially populated following vibrational predissociation of the NO–alkanes. For NO–CH_4 and NO–ethane, the dominant NO population arises from prompt dissociation, whereas the most occupied NO product states from NO–propane and NO–(n-butane) stem from a relatively slower mechanism. Future work will focus on carrying out dynamics simulations on high-level potential energy surfaces to determine the role of a possible geometric phase on the nonadiabatic outcomes.

Conclusions

In summary, we reported the infrared action spectroscopy and infrared-driven dynamics of NO–propane and NO–(n-butane) in the CH stretch region, while also comparing the results to the analogous experiments carried out for NO–CH_4 and NO–ethane. The infrared spectroscopy is analyzed using rovibrational simulations for comparison to experiment and to determine the vibrational predissociation lifetimes of the NO–propane and NO–(n-butane) collision complexes. Due to pseudo Jahn–Teller dynamics, the NO–propane and NO–(n-butane) decay mechanisms from IR activation appear similar to those for NO–ethane. Furthermore, the NO ($X^2\Pi$, $v'' = 0, J'', F_n, \Lambda$) product state distributions from NO–alkane fragmentation reveal a strong electron-spin polarization and a propensity for NO products to rotate in the plane of the π^* molecular orbital, yielding mechanistic insights into the inelastic scattering outcomes. We hypothesize that a geometric phase may be present, impacting the relative population distributions, in addition to the accessible pathway timescales.

Author contributions

PGB: investigation (experiment), writing – reviewing and editing; WCW: investigation (experiment); EM: investigation (experiment); JDB: investigation (experiment); RS: investigation (experiment); JTK: investigation (experiment); NMK: conceptualization (experiment), supervision (experiment), analysis (experiment), writing – original draft.

Data availability

The data supporting this paper have been included as part of the article and ESI.† The electronic structure and vibrational frequency analysis output files can be accessed *via* FigShare, DOI: 10.6084/m9.figshare.26789911.

Conflicts of interest

There are no conflicts to declare.

Acknowledgements

NMK acknowledges support from the donors of the American Chemical Society Petroleum Research Fund (PRF# 65737-UR6) and NSF CAREER award CHE-2239624. The authors also acknowledge William & Mary Research Computing for providing computational resources that contributed to the results reported within this paper.

References

1 J. Liang, L. W. Horowitz, D. J. Jacob, Y. Wang, A. M. Fiore, J. A. Logan, G. M. Gardner and J. W. Munger, Seasonal Budgets of Reactive Nitrogen Species and Ozone over the United States, and Export Fluxes to the Global Atmosphere, *J. Geophys. Res.: Atmos.*, 1998, **103**, 13435–13450.

2 R. Atkinson, Atmospheric Chemistry of VOCs and NO_x, *Atmos. Environ.*, 2000, **34**, 2063–2101.

3 B. Gruber, V. Tajti and G. Czakó, Vibrational Mode-Specific Dynamics of the OH + C_2H_6 Reaction, *J. Phys. Chem. A*, 2023, **127**, 7364–7372.

4 B. Gruber, V. Tajti and G. Czakó, Full-Dimensional Automated Potential Energy Surface Development and Dynamics for the OH + C_2H_6 Reaction, *J. Chem. Phys.*, 2022, **157**, 074307.

5 H. Li, D. Troya and A. G. Suits, Multichannel Dynamics in the OH + *n*-Butane Reaction Revealed by Crossed-Beam Slice Imaging and Quasiclassical Trajectory Calculations, *J. Chem. Phys.*, 2020, **153**, 014302.

6 N. Dias, H. Li and A. G. Suits, Crossed-Beam Imaging of the Reaction of OH with Propanol Isomers, *J. Phys. Chem. A*, 2023, **127**, 5202–5208.

7 P. Liang, E. V. F. de Aragão, L. Giani, L. Mancini, G. Pannacci, D. Marchione, G. Vanuzzo, N. Faginas-Lago, M. Rosi, D. Skouteris, P. Casavecchia and N. Balucani, OH($^2\Pi$) + C_2H_4 Reaction: A Combined Crossed Molecular Beam and Theoretical Study, *J. Phys. Chem. A*, 2023, **127**, 4609–4623.

8 V. M. Tamé-Reyes, A. M. Gardner, J. P. Harris, J. McDaniel and T. G. Wright, Spectroscopy of the Ã State of NO–Alkane Complexes (Alkane = Methane, Ethane, Propane, and *n*-Butane), *J. Chem. Phys.*, 2012, **137**, 214307.

9 J. P. Davis, R. W. Neisser and N. M. Kidwell, Infrared Activated Signatures and Jahn–Teller Dynamics of NO–CH_4 Collision Complexes, *J. Phys. Chem. A*, 2023, **127**, 5171–5182.

10 J. P. Davis, P. G. Burroughs, W. C. Wilkinson, E. Majumdar and N. M. Kidwell, Bimolecular Collision Outcomes on Multidimensional Potential Energy Surfaces: Infrared Spectroscopy and Activation of NO–Alkane Collision Complexes, *Faraday Discuss.*, 2024, **251**, 262–278.

11 V. Dribinski, A. Ossadtchi, V. A. Mandelshtam and H. Reisler, Reconstruction of Abel Transformable Images: The Gaussian Basis-Set Expansion Abel Transform Method, *Rev. Sci. Instrum.*, 2002, **73**, 2634–2642.

12 D. C. Jacobs and R. N. Zare, Reduction of 1 + 1 Resonance Enhanced MPI Spectra to Populations and Alignment Factors, *J. Chem. Phys.*, 1986, **85**, 5457–5468.

13 D. C. Jacobs, R. J. Madix and R. N. Zare, Reduction of 1 + 1 Resonance Enhanced MPI Spectra to Population Distributions – Application to the NO ($A^2\Sigma^+$)–($X^2\Pi$) System, *J. Chem. Phys.*, 1986, **85**, 5469–5479.

14 J. Luque and D. R. Crosley, *LIFBASE: Database and Spectral Simulation Program*, 2013.

15 M. J. Frisch, G. W. Trucks, G. W. Schlegel, G. E. Scuseria, M. A. Robb, J. R. Cheeseman, G. Scalmani, V. Barone, G. A. Petersson and H. Nakatsuji, *et al. Gaussian 16, Revision C.01*.

16 J. Contreras-García, E. R. Johnson, S. Keinan, R. Chaudret, J. P. Piquemal, D. N. Beratan and W. Yang, NCIPLOT: A Program for Plotting Noncovalent Interaction Regions, *J. Chem. Theory Comput.*, 2011, **7**, 625–632.

17 S. W. Sharpe, T. J. Johnson, R. L. Sams, P. M. Chu, G. C. Rhoderick and P. A. Johnson, Gas-Phase Databases for Quantitative Infrared Spectroscopy, *Appl. Spectrosc.*, 2004, **58**, 1452–1461.

18 C. M. Western and B. E. Billinghurst, Automatic and Semi-Automatic Assignment and Fitting of Spectra with PGOPHER, *Phys. Chem. Chem. Phys.*, 2019, **21**, 13986–13999.

19 D. R. Lide Jr., Microwave Spectrum, Structure, and Dipole Moment of Propane, *J. Chem. Phys.*, 1960, **33**, 1514–1518.

20 CCCBDB calculated rotational constants page 3m. **https://cccbdb.nist.gov/rotcalc2x.asp** (accessed 2024-06-01). Using the calculated results at the DFT/ω97X-D/6-311+G(d,p) level.

21 Constants of Diatomic Molecules in NIST Chemistry WebBook, NIST Standard Reference Database Number 69; National Institute of Standards and Technology: Gaithersburg MD, 20899, 2023.

22 R. Crespo-Otero, R. Suardiaz, L. A. Montero and J. M. García de la Vega, Potential Energy Surfaces and Jahn–Teller Effect on CH_4–NO Complexes, *J. Chem. Phys.*, 2007, **127**, 104305.

23 J. Liu, Rotational and Fine Structure of Open–Shell Molecules in Nearly Degenerate Electronic States, *J. Chem. Phys.*, 2018, **148**, 124112.

24 J. A. Beswick and J. Jortner Intramolecular Dynamics of van der Waals Molecules, *Advances in Chemical Physics*, John Wiley & Sons, Ltd, 1981, pp. 363–506.

25 G. E. Ewing, Selection Rules for Vibrational Energy Transfer: Vibrational Predissociation of van der Waals Molecules, *J. Phys. Chem.*, 1987, **91**, 4662–4671.

26 P. Andresen and E. W. Rothe, Analysis of Chemical-Dynamics *Via* Λ-Doubling – Directed Lobes in Product Molecules and Transition States, *J. Chem. Phys.*, 1985, **82**, 3634–3640.

27 Y. Wu, G. Miao and J. E. Subotnik, Chemical Reaction Rates for Systems with Spin–Orbit Coupling and an Odd Number of Electrons: Does Berry's Phase Lead to Meaningful Spin-Dependent Nuclear Dynamics for a Two State Crossing?, *J. Phys. Chem. A*, 2020, **124**, 7355–7372.

28 Y. Wu and J. E. Subotnik, Electronic Spin Separation Induced by Nuclear Motion near Conical Intersections, *Nat. Commun.*, 2021, **12**, 700.

29 M. Zhang, X. Mi, L. Zhang, C. Wu, H. Xu and Z. Li, Observing a Berry Curvature Effect in CH_2OH Photodissociation *via* Molecular Dynamics Simulations, *Phys. Rev. B: Condens. Matter Mater. Phys.*, 2024, **109**, 184304.